

Document downloaded from:

<http://hdl.handle.net/10251/104484>

This paper must be cited as:

Bayón Barrachina, A.; Toro, J.; Bombardelli, F.; Matos, J.; López Jiménez, PA. (2017). Influence of VOF technique, turbulence model and discretization scheme on the numerical simulation of the non-aerated, skimming flow in stepped spillways. *Journal of Hydro-Environment Research (Online)*. 19:137-149. doi:10.1016/j.jher.2017.10.002



The final publication is available at

<http://doi.org/10.1016/j.jher.2017.10.002>

Copyright Elsevier

Additional Information

1 **Influence of VOF technique, turbulence model and discretization scheme on the numerical**
2 **simulation of the non-aerated, skimming flow in stepped spillways**

3
4 Arnau Bayon,^{1,*} Juan Pablo Toro,² Fabián A. Bombardelli,³ Jorge Matos,⁴ and Petra Amparo
5 López-Jiménez⁵

6 ¹Research Institute of Water and Environmental Engineering (IIAMA). Universitat Politècnica
7 de València, Camí de Vera, s/n, 46022, València, Spain (arbabar@iiama.upv.es)

8 ²Assistant Professor, Department of Civil Engineering, Universidad Andres Bello, Santiago
9 8320000, Chile; formerly, Ph.D. Candidate, Department of Civil and Environmental Engineering,
10 Univ. of California, 2001 Ghausi Hall, One Shields Ave., Davis, CA 95616. E-mail:
11 juan.toro.1@unab.cl

12 ³Department of Civil and Environmental Engineering, University of California, Davis, USA
13 (fabianbombardelli2@gmail.com)

14 ⁴Department of Civil Engineering, Architecture and Georesources, Instituto Superior Técnico,
15 Universidade de Lisboa, Av. Rovisco Pais 1, 1049-001, Lisboa, Portugal
16 (jorge.matos@tecnico.ulisboa.pt)

17 ⁵Department of Hydraulic and Environmental Engineering, Universitat Politècnica de València,
18 Camí de Vera, s/n, 46022, València, Spain (palopez@upv.es)

19 *Corresponding author

20
21
22 **Abstract**

23
24 An accurate description of the hydrodynamics in the non-aerated region of the skimming flow on
25 stepped spillways is of utmost importance, particularly in small structures at large discharges. In
26 addition, the flow features upstream of the inception point of air entrainment determine the flow
27 behavior in the downstream self-aerated region. In this work, numerical models of the flow in the
28 non-aerated region of stepped spillways have been developed using diverse turbulence closures
29 and discretization schemes implemented in two CFD codes: *OpenFOAM* and *FLOW-3D*[®]. Partial
30 VOF (Volume of Fluid) and “True” VOF (*TruVOF*) approaches are employed to capture the
31 position of the free surface. The Standard, RNG and Realizable k - ε , in addition to the SST k - ω

32 model, are used for turbulence closure. Numerical results are compared against reference
33 experimental results obtained from a physical model of constant slope of 0.75H:1V. Models with
34 turbulence closures of the $k-\varepsilon$ family provide nearly the same predictions for the mean flow
35 velocity with maximum differences on average smaller than 1%. Regarding discretization schemes,
36 the first-order upwind method provides predictions for the mean flow velocity which are not
37 significantly different (within 6%) than those obtained with second-order counterparts. However,
38 these differences can be larger when maximum values of turbulent kinetic energy (TKE) and
39 dissipation rate of TKE at the step edges are compared. In spite of the fact that the *TruVOF*
40 (*FLOW-3D*[®]) method does not account for the tangential stresses at the air-water interface,
41 differences in the tracking of the free surface position among this method and the Partial VOF
42 method (*OpenFOAM*) were found to be smaller than 3% along the stepped spillway. In this work,
43 we also provide a physical interpretation of the flow results.

44

45 **Keywords:** Stepped spillway; Computational Fluid Dynamics (CFD); *OpenFOAM*; *FLOW-3D*;
46 RANS; VOF.

47

48 **1. Introduction**

49

50 Stepped spillways have been used for centuries as multi-purpose hydraulic structures: flow
51 energy dissipation, aesthetics, flood evacuation, etc. (Chanson, 2002). It was not until last century,
52 in concomitance with the spreading of new construction methodologies, such as roller compacted
53 concrete (RCC), that stepped spillways became an appealing way to dissipate energy (Chanson et
54 al., 2015; Matos & Meireles, 2014).

55 The presence of macro-roughness elements increases the rate of boundary-layer development
56 in the stepped spillway, thus displacing upstream the inception point of air entrainment; i.e., the
57 section where the boundary layer encounters the water free surface and eddies possess enough
58 energy to distort it (Meireles et al., 2014).

59 So far, most of the studies in the literature have been based on experimental modeling in the
60 self-aerated, skimming flow region (see e.g., Chanson, 2002; Matos & Meireles, 2014; Chanson et
61 al., 2015). Such studies have been able to provide clear insight into relevant subjects, such as
62 location of the inception of air entrainment, air concentration and velocity distributions, pressure
63 distribution on the step faces, flow resistance and energy dissipation.

64 The quantity of studies dealing with the non-aerated part of the flow is limited (Amador, 2005;
65 Amador et al., 2006; Bombardelli et al., 2011; Carvalho & Amador, 2009; Hunt & Kadavy, 2010;
66 Meireles & Matos, 2009; Toro et al., 2016; Zhang & Chanson, 2016a, 2016b). This fact is to a
67 certain extent justified, as on most prototype applications self-aeration would occur in a
68 considerable portion of the chute for the design discharge. Nevertheless, in some real-life cases,
69 especially in small structures at large discharges, the non-aerated flow can dominate most of the
70 length of the flow (Bombardelli et al., 2011; Meireles et al., 2014). Characterizing the non-aerated
71 region of the flow is also important with regard to cavitation. Recent studies showed that if flow
72 velocities in the non-aerated skimming flow region are large enough, cavitation and related
73 damage on the step surfaces may occur (Frizell et al. 2013, 2015). In addition, an accurate
74 description of maximum velocities and turbulence statistics close to the inception point of air
75 entrainment is crucial for the understanding of the flow features downstream of the inception point
76 (Toro et al., 2016). To the best of the Authors' knowledge, a full and comprehensive description of
77 the flow features in the aerated zone has not been achieved so far.

78 Recent numerical works focusing on the non-aerated region have provided good predictions of
79 time-averaged velocities, water depths, development of the boundary layer and turbulence statistics
80 (Bombardelli et al., 2011; Meireles, 2011; Toro et al., 2016). However, relatively little emphasis
81 has been put into the influence of the VOF technique, the turbulence closure and the discretization
82 schemes on the numerical results. There is the natural question as to whether these variables exert
83 significant differences in the prediction of the main flow properties in such region. In this paper, a
84 new two-dimensional (2D) CFD model of the skimming flow in the non-aerated region on stepped
85 spillways is presented. Incompressible turbulent flow is assumed and the free surface is captured
86 by means of Partial- and Complete-VOF methods (Bombardelli et al., 2001; Hirt & Nichols, 1981).
87 The theoretical model is implemented in the open source toolbox *OpenFOAM* and the numerical
88 results are compared against a dataset collected at a facility assembled at the National Laboratory
89 of Civil Engineering (LNEC), in Lisbon, Portugal, available in Matos (1999), Meireles (2004,
90 2011), and Renna (2004). Further, those numerical data are compared with counterparts obtained
91 with the use of the code *FLOW-3D*[®] (Bombardelli et al., 2011). A model sensitivity analysis to
92 different turbulence closures and discretization schemes is performed and discussed. To the best of
93 the Authors' knowledge, such a thorough comparison among different VOF approaches,
94 turbulence models and discretization schemes to determine which of them performs best has not
95 been conducted so far. The flow self-similarity at various locations of the spillway is also assessed
96 by analyzing the flow turbulence properties.

97 It is believed that results of this research provides answers regarding very-important, current
98 discussions on how to model the non-aerated portion of stepped spillways, given the theoretical
99 models included in some codes and packages.

100

101 **2. Experimental data**

102

103 The experimental facility used for validation of the numerical model presented herein was built
104 at LNEC, in Lisbon, Portugal. The experimental results have been already published elsewhere
105 (e.g., Meireles, 2004, 2011; Bombardelli et al., 2011; Meireles et al., 2012, 2014), so only a brief
106 summary is provided in this section.

107 The facilities consisted of a reservoir, and a smooth crest following the profile of the
108 Waterways Experimental Station (WES). The first steps downstream of the crest had variable size
109 for their edges to fit the WES profile, as depicted in Fig. 1. A tangent point was defined
110 downstream, where the WES profile presented uniform steps. These steps were 3 cm long and 4
111 cm tall, defining a chute slope of 1V:0.75H. The total height of the device, from crest to toe, was
112 2.9 m and had a constant width of 1 m.

113 Measurements were taken using a conductivity probe and a back-flushing Pitot tube held in
114 such a way that measurements could be taken parallel to the spillway pseudo-bottom (see Fig. 2).
115 Even though this work focuses on the non-aerated region of the flow, air concentration
116 measurements helped both to determine the equivalent clear-water depth and to correct
117 differential pressure data in the wavy region. A more thorough discussion on the experimental
118 setup is available in Matos (1999), Meireles (2004, 2011), Renna (2004), Bombardelli et al.
119 (2011), and Meireles et al. (2012, 2014). For the current paper, data presented in Bombardelli et
120 al. (2011), and collected in the framework of Meireles (2004), was considered for the
121 comparative analysis.

122

123

124 3. Theoretical and numerical models

125

126 3.1 Flow model

127 In cases where large domains have to be modeled and no special attention is paid to what
128 occurs at very small time and spatial scales, which generally takes place in most engineering
129 applications, the turbulence averaging of the flow variables in the Navier-Stokes Equations, the so-
130 called Reynolds-Averaged Navier-Stokes (RANS), constitutes the best choice. The RANS
131 Equations [Eqs. (1) and (2) below] are thus solved in this paper. The mass and momentum
132 equations are expressed in vector/tensor notation in the following form, respectively:

$$133 \nabla \cdot \underline{\underline{u}} = 0 \quad (1)$$

$$134 \frac{\partial \underline{\underline{u}}}{\partial t} + \underline{\underline{u}} \cdot \nabla \underline{\underline{u}} = -\frac{1}{\rho} \nabla \bar{p} + \frac{1}{\rho} \nabla \cdot (\underline{\underline{\tau}} + \underline{\underline{\tau}}^R) + \bar{\underline{\underline{f}}}_b \quad (2)$$

135 where $\underline{\underline{u}}$ is the time-averaged velocity vector, \bar{p} is pressure, ρ indicates the density, t is time, $\underline{\underline{\tau}}$
136 refers to the averaged, deviatoric stress tensor, $\underline{\underline{\tau}}^R$ is the Reynolds stress tensor and $\bar{\underline{\underline{f}}}_b$ is the
137 gravity force. Surface tension was not included because Weber numbers were always above 110
138 (see Boes & Hager, 2003), thus indicating that this force does not exert a large effect on the flow.

139

140 3.2 Free surface modeling

141

142 One of the most widely-used methods to capture the position of the free surface is the so-called
143 VOF (Volume of Fluid) method, developed by Hirt and Nichols (1981). This technique is based on
144 three elements: a) the definition of the volume of fluid function (α), which is equal to one when the
145 computational volume is occupied by water, zero when it is air and in between zero and one when
146 the volume is occupied by both air and water; b) the imposition of boundary conditions (i.e.,

147 pressure) at the unknown free surface; and c) the use of an accurate numerical scheme to avoid
 148 numerical diffusion of the free surface solution (Bombardelli et al., 2001). Small variants of this
 149 method (improvements) are implemented in *FLOW-3D*[®], named as TruVOF by the developers
 150 (*FLOW-3D*[®] User Manual, 2016), and those variants have demonstrated their validity in a wide
 151 range of hydraulic engineering applications (Bombardelli et al., 2001, 2011; Rodríguez et al.,
 152 2004). The VOF method implemented in *FLOW-3D*[®] has all three ingredients mentioned above. In
 153 particular, the implementation of free-surface boundary conditions requires special care to avoid
 154 numerical instabilities; further, from the physical point of view, it better reflects the fact that, with
 155 the exception of a (thin) boundary layer, water and air generally move independently of each other.

156 In other codes in general, and in *OpenFOAM* in particular, a “Partial” VOF is employed, where
 157 both the water and air flows are solved (Bombardelli et al., 2001). This approach presents certain
 158 advantages such as accounting for air-water shear stresses; however, it increases the model overall
 159 computational cost and may introduce erroneous descriptions in some cases, namely, the
 160 simulation of jets coming out of nozzles (Bombardelli et al., 2001).

161 In the TruVOF, the transport of α in the simulated domain is represented by using the
 162 following advection equation:

$$163 \quad \frac{\partial \alpha}{\partial t} + \nabla \cdot (\underline{\underline{u}} \alpha) = 0 \quad (3)$$

164 where $\underline{\underline{u}}$ is the velocity of water. In the Partial VOF method implemented in *OpenFOAM*, the
 165 velocity $\underline{\underline{u}}$ is the shared velocity of the two-phase flow. In this Partial VOF method, all variables in
 166 each volume, e.g., ξ , are weighted according to the fluid fraction for each fluid A and B:

$$167 \quad \xi = \xi_A \alpha + \xi_B (1 - \alpha) \quad (4)$$

168 In the case of *OpenFOAM*, an extra velocity term is added perpendicularly to the water free surface
 169 to help to compress it: $\nabla \cdot (\underline{\underline{u}}_c \alpha [1 - \alpha])$. The term $\alpha [1 - \alpha]$ ensures that the compression velocity

170 only affects those regions where flow fractions are close to 0.5 (Rusche, 2002). The compression
171 velocity term is computed according to a method based on the theory of two-phase flow
172 (Berberovic et al., 2009):

$$173 \quad \underline{u}_c = |\underline{u}| \frac{\nabla \alpha}{|\nabla \alpha|} \quad (5)$$

174 where $|\underline{u}|$ is the mixed flow velocity modulus, although in Berberovic et al. (2009), the term \underline{u}_c
175 represents the relative velocity between both phases, $\underline{u}_w - \underline{u}_a$.

176 The free surface position is usually defined at the point where $\alpha = 0.5$. More information on free
177 surface modeling can be found in Ubbink (1997), Bombardelli et al. (2001), Rusche (2002) and
178 Berberovic (2010).

179

180 3.3. Turbulence modeling

181

182 Four different turbulence closures are employed in this work, keeping all the other parameters
183 constant, and their results are analyzed and compared. The four assessed models are the Standard
184 k- ϵ (Launder & Sharma, 1974), the Realizable k- ϵ (Shih et al., 1995), the RNG k- ϵ (Yakhot et al.,
185 1992), and the SST k- ω (Menter, 1993). The models of the k- ϵ family have proven to yield good
186 results in the modeling of hydraulic structures (Bayon et al., 2016; Bayon & López-Jiménez, 2015;
187 Bombardelli, 2004; Bombardelli et al., 2011; Bradshaw, 1996; Romagnoli et al., 2009; Witt et al.,
188 2015), whereas the SST k- ω model has been successfully applied by the Authors in a study of a
189 hydraulic jump (Bayon & López-Jiménez, 2015).

190 The comparative analysis is conducted exclusively using the RNG k- ϵ simulations, so that the
191 numerical data obtained with *OpenFOAM* are equivalent to the results obtained by Bombardelli et
192 al. (2011) using *FLOW-3D*[®]. The RNG k- ϵ model is a two-equation turbulence model based on the

193 concept of eddy viscosity ($\nu_t = \frac{\mu_t}{\rho}$), where the two additional variables to compute it are k
 194 (turbulent kinetic energy, TKE) and ε (dissipation rate of TKE). The transport of these two
 195 variables is modeled according to the following advection-diffusion-reaction (ADR) equations:

$$196 \quad \frac{\partial}{\partial t}(\rho k) + \nabla \cdot (\rho k \bar{\mathbf{u}}) = \nabla \cdot \left[\left(\mu + \frac{\mu_t}{\sigma_k} \right) \nabla k \right] + P_k - \rho \varepsilon \quad (5)$$

$$197 \quad \frac{\partial}{\partial t}(\rho \varepsilon) + \nabla \cdot (\rho \varepsilon \bar{\mathbf{u}}) = \nabla \cdot \left[\left(\mu + \frac{\mu_t}{\sigma_\varepsilon} \right) \nabla \varepsilon \right] + (C_{1\varepsilon} - R) \frac{\varepsilon}{k} P_k - C_{2\varepsilon} \rho \frac{\varepsilon^2}{k} \quad (6)$$

$$198 \quad R = \eta(-\eta/\eta_0 + 1)/(\beta\eta^3 + 1); \quad \eta = S k/\varepsilon; \quad S = (2\bar{S}_{ij}\bar{S}_{ij})^{1/2} \quad (7)$$

199 where P_k is the production of TKE and \bar{S}_{ij} is the strain-rate tensor. The formulation constants are
 200 $\sigma_k = 0.7194$, $\sigma_\varepsilon = 0.7194$, $c_{1\varepsilon} = 1.42$, $c_{2\varepsilon} = 1.68$, $C_\mu = 0.0845$, $\eta_0 = 4.38$, and $\beta = 0.012$.

201 The eddy viscosity is computed as $\nu_t = C_\mu \frac{k^2}{\varepsilon}$.

202

203 3.4. Boundary conditions

204

205 The boundary conditions imposed to the model are as follows. At the inlet, a constant-depth
 206 subcritical flow is followed by a stretch of reservoir of 1.2m in length (measured from the
 207 boundary to the crest of the spillway). This buffer zone is long enough according to the Authors'
 208 experience (Bombardelli et al., 2011; Toro et al., 2016). Downstream of the spillway, an outlet
 209 boundary condition is imposed, where the flow leaves the domain in supercritical state. With
 210 regards to the turbulence model variables, k, ε and ω , no measurements are available at the
 211 reservoir entrance. Therefore, a Dirichlet boundary condition is set to a low value for the actual
 212 profiles to develop along the reservoir buffer stretch.

213 The upper boundary condition of the model is atmospheric and so the flow can freely enter or
 214 exit the domain through it; all variables are set to a null von Neumann boundary condition, except

215 for pressure, which is set to atmospheric. A smooth no-slip boundary condition is applied to the
216 solid contours of the model (the roughness of the methacrylate of the experimental device is
217 negligible). Additionally, wall functions are imposed to the solid boundaries in the k- ϵ family
218 models. The values of y^+ throughout the entire chute were such that the first node was located
219 outside of the viscous sub-layer, thus ensuring that the wall function was operating as intended.
220 Therefore, all mesh elements in contact with solid boundaries have a y^+ coordinate at the
221 logarithmic layer, i.e. $y^+ \in [30,100]$ (Ferziger & Peric, 2012; Schlichting & Gersten, 2000). The
222 y^+ variable is defined as $y^+ = y \frac{u_\tau}{\nu}$, where y is the distance of the center of the first volume to the
223 wall, u_τ is the shear velocity, and ν is the kinematic viscosity. On the other hand, since the SST k-
224 ω is a low-Reynolds model, a mesh refinement is required for all mesh volumes in contact with
225 solid boundaries, so that the first volume is in the viscous sub-layer.

226

227 3.5. Numerical schemes

228

229 The numerical solution of the equations presented above was developed via the finite-volume
230 method (FVM), and implemented in the code *OpenFOAM* (*OpenFOAM* User Guide, 2011). In
231 *OpenFOAM*, the numerical integration is conducted using the PIMPLE algorithm, a combination
232 of two widely used algorithms: PISO (Issa, 1985) and SIMPLE (Patankar & Spalding, 1972).

233 In the present work, three different discretization schemes are used to approximate the
234 advection terms: a) a first-order upwind method; b) the second-order limited Van Leer (1977)
235 method; and c) a second-order limited central difference method. A sensitivity analysis to the
236 numerical discretization scheme is conducted along with the rest of model parameters.

237 Time derivatives are discretized using a second-order backward discretization scheme. The
238 diffusive terms of the equations are discretized using a second-order accurate Gauss linear
239 corrected scheme in all cases.

240

241 **4. Model implementation**

242

243 *4.1. Geometry and mesh*

244

245 A structured mesh formed by rectangular elements of 4/3 aspect ratio was employed, as was
246 done in Bombardelli et al. (2011). The mesh employed in the SST k- ω simulations required
247 additional refinement in the near-wall region to ensure that y^+ remains within the viscous sub-
248 layer. To this end, 10 extra layers of total thickness equal to 1/3 of the normal element size and a
249 growth ratio of 1.175 were added to the elements adjacent to the spillway steps.

250 In order to fit the mesh to the modeled geometry, the OpenFOAM model uses the tool
251 *snappyHexMesh*; its use in similar applications has yielded good results (Sweeney, 2014; Toro et
252 al., 2016). The *FLOW-3D*[®] code uses the porosity-based FAVOR method to define solid objects,
253 which, if correctly used, yields accurate results (Bombardelli et al., 2011; Carvalho et al., 2008).

254 To obtain mesh-independent results, 5 different mesh sizes were used and the grid convergence
255 index (GCI) methodology proposed by Roache (2009) was employed. This procedure, based on the
256 Richardson Extrapolation, is discussed and exemplified in Celik et al. (2008). The grid refinement
257 degree between consecutive sizes is $r = \sqrt{2}$, thus being the global refinement degree $r_g = 4.0$,
258 above the 1.3 minimum value proposed by Celik et al. (2008). Mesh refinement is conducted
259 systematically using $h = \sqrt{\Delta x \Delta y}$ as mesh size indicator. The characteristics of the tested meshes

260 are summarized in Table 1. Water depths (d) at 6 different locations are used as indicator variables
 261 to compute the residual error among successive mesh sizes. Fig. 3 shows mesh number 5 in the
 262 crest zone as an example.

263

Mesh number	Horiz. size (Δx) (mm)	Vert. size (Δy) (mm)	Aspect ratio (V/H)	$h = \sqrt{\Delta x \Delta y}$ (mm)
1	1.06	1.41	4/3	1.22
2	1.50	2.00	4/3	1.73
3	2.12	2.83	4/3	2.45
4	3.00	4.00	4/3	3.46
5	4.24	5.66	4/3	4.90

264 **Table 1.** Characteristics of the meshes tested in the convergence analysis.

265

266 Simulations were compared against the LNEC experimental data for a discharge of $0.18\text{m}^3/\text{s}$
 267 (specific discharge of $0.18\text{m}^2/\text{s}$). These simulations were run varying only one parameter from one
 268 simulation to another in order to capture the effect of that specific parameter.

269

270 5. Analysis of results

271

272 5.1. Mesh convergence

273

274 The mesh-convergence analysis was conducted using the results obtained with a first-order
 275 discretization scheme, as this was the setup used in Bombardelli et al. (2011). In Fig. 4, a

276 comparison of water free surface profiles for $\alpha = 0.5$ obtained with different mesh sizes is shown.
277 The apparent order reaches a value of $p_{k-\varepsilon} = 0.927$ and $p_{k-\omega} = 0.924$ for the RNG k- ε model
278 and the SST k- ω model, respectively, both close to the model formal order in mesh number 2
279 ($h = 1.73mm$), which indicates that the asymptotic range has been reached. The analysis of these
280 meshes indicates that the average approximate relative error in the indicator variables was
281 $e_{\alpha(k-\varepsilon)} = 3.7\%$ and $e_{\alpha(k-\omega)} = 3.4\%$. The grid convergence index was $GCI_{k-\varepsilon} = 4.9\%$ and
282 $GCI_{k-\omega} = 4.4\%$, respectively, revealing that in both cases numerical uncertainty remains within
283 acceptable ranges as used in the literature. None of the indicator parameters of the mesh
284 convergence analysis shows improvement at sizes below the size of mesh number 2 ($h =$
285 $1.73mm$). All subsequent analyses are conducted on results employing the mesh of $h = 1.73mm$.

286 Clearly, both codes, *OpenFOAM* and *FLOW-3D*[®], respond differently to mesh size reduction.

287

288 5.2. Sensitivity analysis

289

290 This analysis was exclusively conducted using *OpenFOAM* results, as *FLOW-3D*[®] results have
291 already been analyzed in Bombardelli et al. (2011).

292 As expected, second-order methods yield more accurate results than their first-order
293 counterparts; however, all schemes tend to underestimate mean flow velocities with a consistent
294 overestimation of flow depths. Differences between first- and second-order methods are small
295 when predicting these variables (4%), but they reach larger values (not shown herein) when
296 predicting maximum TKE on step edges. The differences in the model outcome are small among
297 different second-order discretization schemes (Fig. 5): both limited central-difference and limited
298 Van Leer discretization schemes yield differences in estimations below 4% compared to

299 experimental data for all the analyzed variables. Nevertheless, the limited central-difference
300 scheme seems to systematically achieve accuracies between 5% and 10% higher employing
301 approximately 30% smaller computational times than the Van Leer scheme.

302 With regard to turbulence models, it is shown in Fig. 6 that the RNG k- ϵ , the Standard k- ϵ and
303 the Realizable k- ϵ models yield virtually the same results (differences are on average below 1%),
304 as expected. On average terms, a slightly better performance can be attributed to the RNG k- ϵ
305 model in the prediction of certain variables, such as water depths or the profiles within the
306 boundary layer, but this difference is not rather small. As depicted in Fig. 6, the SST k- ω model
307 tends to overestimate water depths (4%) with a consistent underestimation of velocities slightly
308 above the SST k- ϵ (2% overestimation of water depths). It can also be observed how the latter
309 model yields more developed velocity profiles than the SST k- ω models, although these
310 differences become insignificant when predicting velocity profiles within step cavities.

311

312 *5.3. Discussion of approaches and self-similarity analysis*

313

314 The flow depth throughout the stepped spillway is very well predicted by all approaches (see
315 Fig. 7). The first reach located over the smooth region near the spillway crest is reproduced with a
316 root mean square error (RMSE) below 1%. In the last steps, all approaches seem to overestimate
317 the experimental results, although results with TruVOF are slightly closer to the experimental data.
318 The RMSE in the water profile estimation for the TruVOF method is 4.2%, slightly below the
319 6.2% attained by the Partial VOF.

320 With regards to velocity profiles, the formation of a boundary layer is accurately captured by
321 both methodologies (see Fig. 8), although rather significant differences can be observed among

322 them. For example, the Partial VOF predicts more developed boundary layers than the TruVOF.
323 Both approaches tend to slightly underestimate the velocity values, although the Partial VOF
324 achieves a smaller difference with the experimental data than the TruVOF method. This may be
325 due, among other causes, to the fact that the TruVOF does not account for free-surface tangential
326 stresses. In both cases, this velocity underestimation is consistent with the overestimation of flow
327 depths discussed above.

328 Compared to the velocity profiles obtained through a very recent three-dimensional (3D)
329 detached eddy simulation (Toro et al., 2017), the velocity profiles obtained in this work are very
330 close to those of 3D simulations, confirming that the 2D approach can give useful results for most
331 engineering purposes, and 3D results can be reserved for research.

332 In Fig. 9, the evolution of flow depths and boundary-layer development for both Partial VOF
333 and TruVOF methods is presented. By extrapolating their trending curves, the approximate
334 location of the inception point, i.e., where flow aeration starts, can be estimated. According to this
335 extrapolation, Partial VOF predicted a distance to the inception point of 1.66m, whereas the
336 TruVOF estimated 1.87m. Compared to the experimentally observed distance to the inception
337 point, Partial VOF and TruVOF overestimated this variable by 14% and 30%, respectively. It bears
338 emphasis that the experimental data have uncertainties on its own given the difficulty of
339 determining the precise location of the inception point due to unsteadiness.

340 The experimental results and the inception point location computed according to Chanson
341 (2002) are also included in Fig. 9. Compared to this dataset, the results of Partial VOF and TruVOF
342 differ with experiments in 2% and 7%, respectively, which is indeed accurate enough for
343 engineering purposes. A recent experimental work (Zhang & Chanson, 2016a) states that the
344 inception point occurs where the boundary layer thickness reaches 80% of the water depth. Using

345 this criterion, the Partial VOF and TruVOF estimate distances to the inception point of 1.33m and
346 1.28m, respectively. Compared to the experimental data, the models underestimated this variable
347 by 8% and 12%, respectively. Toro et al. (2017) have very recently shown that cylindrical vortex
348 tubes develop and evolve with space throughout the boundary layer growth, being responsible for
349 the perturbations of the free surface which lead to air entrainment. The complex nature of these
350 tubes can help understand the typical unsteadiness observed in the laboratory experiments and the
351 difficulty of predicting the location of the inception point with accuracy.

352 As discussed above, a certain trend to yield more developed velocity profiles near the spillway
353 crest is observed from the computations using Partial VOF, resulting in a clear overestimation of
354 the boundary-layer thickness within this region ($L < 0.75m$).

355 Meireles (2011) and Toro et al. (2016) proposed and corroborated self-similarity of turbulence
356 statistics in stepped spillways, an unprecedented result. Similarly, Felder and Chanson (2011)
357 discussed self-similarity of the integral time scales in terms of similar trends in the flow
358 distributions along the cavity. However, there was no clear description of the self-similarity in the
359 flow velocity within the cavity, as no negative velocities were recorded in the recirculation region.
360 Previously, in Gonzalez and Chanson (2004), similar trends of the flow velocity within the cavity
361 were presented; in that study, non-dimensional velocities were obtained by using the velocity at
362 which half of the freestream velocity is reached.

363 In the case presented herein, the results show the occurrence of a certain pattern in the velocity
364 and TKE distributions throughout the spillway (see Fig. 10). Using a suitable normalization, most
365 of flow variables present self-similar behavior throughout the spillway. This fact was investigated
366 by using exclusively *OpenFOAM* data and the results indicate approximate flow self-similarity.

367 Fig. 11 shows the normalized profiles of velocity, TKE, dissipation rate and pressure at
368 different step edges compared with the results reported in previous works for the velocities. These
369 profiles show an important degree of overlapping. Additionally, it was observed that the highest
370 pressures always occur close to the pseudo-bottom at approximately 0.32cm upstream of the step
371 edges (cf. also with Toro et al., 2016).

372 A self-similar behavior can also be observed in the step cavities, as depicted in Fig. 12,
373 although the differences in the velocity profiles discussed above are not apparent. The velocity
374 profiles predicted by the model in the recirculation zone attain an accuracy of 93.3%, compared to
375 data by Amador et al. (2006). The same authors state that the maximum recirculation velocity is
376 15% of U_{\max} , which is confirmed by the results presented herein. With regards to pressure
377 profiles, it can be observed that this variable drastically drops below the hydrostatic profile in the
378 recirculation region, even attaining negative values, as reported in Toro et al. (2016). It can also be
379 observed that this pressure drop reaches higher values as the distance to the crest increases.

380 Concerning the TKE and dissipation rate of TKE profiles, a peak can be neatly identified near
381 the pseudo-bottom, thus corroborating that the flow in the pseudo-bottom vicinity is responsible for
382 the highest dissipation rates of TKE (Toro et al., 2016, 2017). It was also observed that the
383 dissipation rate profiles perfectly reproduce the shape of the integral turbulent length scale profiles
384 reported in Amador et al. (2006). Toro et al. (2016, 2017) additionally found in the 3D detached
385 eddy simulations that the pseudo-bottom is where vorticity and production of TKE both present a
386 peak, highlighting the tremendous importance of such plane in shedding the tubular structures
387 which are responsible for the deformation of the free surface and, thus, for the air entrainment.

388

389 **6. Final remarks and conclusions**

390 A numerical model, able to reproduce the behavior of the non-aerated region of the flow in
391 stepped spillways, has been implemented using *OpenFOAM*. For its validation, experimental
392 data previously collected at LNEC were used. After conducting a mesh-convergence analysis,
393 the sensitivity to turbulence model, treatment of the free surface and numerical discretization
394 scheme was assessed.

395 Numerical results indicate that the use of a Partial VOF instead of the TruVOF does not
396 affect decisively the predictions of flow velocities and turbulence statistics, although more
397 accurate results can be attributed to the Partial VOF. This result is especially important given the
398 imposition of boundary conditions at the free surface in the TruVOF, which makes it the most
399 cost-effective choice in terms of computational expenses in cases where no strong air-water
400 interaction is expected.

401 The results obtained with several RANS $k-\epsilon$ turbulence models indicate that their predictions
402 of virtually all variables differ less than 1%. The RNG $k-\epsilon$ model performs marginally better,
403 whereas the Standard $k-\epsilon$ and the Realizable $k-\epsilon$ yield virtually the same results. The SST $k-\omega$
404 model, in turn, overestimates the water depths by 4%, with a consistent underprediction of
405 velocities. Differences are more important than those obtained with the models of the $k-\epsilon$ family
406 while solving the flow within the viscous sub-layer. This suggests, at least for this particular case,
407 the benefit of using the RNG $k-\epsilon$ for its smaller computational cost and higher accuracy
408 compared to the SST $k-\omega$.

409 The model sensitivity to different numerical discretization schemes shows that the limited
410 central-difference scheme performs slightly better and at smaller computational costs than the
411 limited Van Leer model, although both second-order schemes yield similar results for velocities

412 and water depths. Its larger accuracy and low computational cost compared to other second-order
413 schemes makes the limited central-difference the most suitable scheme for cases of this nature.

414 Finally, the approximate self-similar behavior of turbulence quantities for the flow on
415 stepped spillways, proposed by our research group elsewhere, was further confirmed in this
416 paper. It was also found that the pressure near step edges raises above the hydrostatic profile,
417 being the maximum value slightly upstream of the step edge. Additionally, special attention is
418 placed on the flow self-similarity within the step cavities, finding that the model presented herein
419 correctly reproduces the data available in the literature for recirculation velocities.

420

421 **Acknowledgments**

422 This study was made possible due to the financial support of the PhD program “VALi+D”,
423 funded by Generalitat Valenciana (Spain).

424 The second author acknowledges the support of the National Commission for Scientific and
425 Technological Research (CONICYT), through a “Becas Chile” fellowship.

426

427

428 **References**

429 Amador, A., 2005. Comportamiento hidráulico de los aliviaderos escalonados en presas de
430 hormigón compactado. Universitat Politècnica de Catalunya, Barcelona (Spain) (in Spanish).

431 Amador, A., Sánchez-Juny, M., Dolz, J., 2006. Characterization of the nonaerated flow
432 region in a stepped spillway by PIV. *J. Fluids Eng.* 128, 1266–1273.

433 Bayon, A., Lopez-Jimenez, P.A., 2015. Numerical analysis of hydraulic jumps using
434 OpenFOAM. *J. Hydroinformatics* 17, 662–678. doi:10.2166/hydro.2015.041

435 Bayon, A., Valero, D., García-Bartual, R., López-Jiménez, P.A., Francisco Jose, V.-M., 2016.
436 Performance assessment of OpenFOAM and FLOW-3D in the numerical modeling of a low
437 Reynolds number hydraulic jump. *Environ. Model. Softw.* 80, 322–335.

438 Berberović, E., van Hinsberg, N.P., Jakirlić, S., Roisman, I.V. and Tropea, C., 2009. Drop
439 impact onto a liquid layer of finite thickness: Dynamics of the cavity evolution. *Physical Review*
440 *E*, 79(3), p.036306.

441 Berberovic E., 2010. Investigation of free-surface flow associated with drop impact:
442 numerical simulations and theoretical modeling, Ph.D. thesis, Technische Universität (Germany).

443 Boes, R.M., Hager, W.H., 2003. Two-phase flow characteristics of stepped spillways. *J.*
444 *Hydraul. Eng.* 129, 661–670.

445 Bombardelli, F.A., Hirt, C.W., García, M.H., Matthews, B.W., Fletcher, C.A.J., Partridge,
446 A.C., Vasquez, S., 2001. Computations of curved free surface water flow on spiral concentrators.
447 *J. Hydraul. Eng.* 127, 629–631.

448 Bombardelli, F.A., Meireles, I., Matos, J., 2011. Laboratory measurements and multi-block
449 numerical simulations of the mean flow and turbulence in the non-aerated skimming flow region
450 of steep stepped spillways. *Environ. Fluid Mech.* 11, 263–288.

451 Bradshaw, P., 1996. Understanding and prediction of turbulent flow. *Int. J. Heat Fluid Flow*
452 18, 45–54.

453 Carvalho, R.F., Amador, A.T., 2009. Physical and numerical investigation of the skimming
454 flow over a stepped spillway. *Adv. Water Resour. Hydraul. Eng.* 1767–1772.

455 Carvalho, R.F., Lemos, C.M., Ramos, C.M., 2008. Numerical computation of the flow in
456 hydraulic jump stilling basins. *J. Hydraul. Res.* 46, 739–752.
457 doi:10.1080/00221686.2008.9521919

458 Celik, I.B., Ghia, U., Roache, P.J., Freitas, C.J., Coleman, H., Raad, P.E., 2008. Procedure
459 for Estimation and Reporting of Uncertainty Due to Discretization in CFD Applications. *J.*
460 *Fluids Eng.* 130, 078001–078001. doi:10.1115/1.2960953

461 Chanson, H., 2002. The hydraulics of stepped chutes and spillways. *Can. J. Civ. Eng.* 29,
462 634–634.

463 Chanson, H., Bung, D., and Matos, J. (2015). Stepped spillways and cascades, in *Energy*
464 *Dissipation in Hydraulic Structures*. IAHR Monograph, CRC Press, Taylor and Francis Group,
465 Leiden, The Netherlands, H. CHANSON Editor, pp. 45-64 (ISBN 978-1-138-02755-8). (Record
466 at UQeSpace).

467 Felder, S., Chanson, H., 2009. Energy dissipation, flow resistance and gas-liquid interfacial
468 area in skimming flows on moderate-slope stepped spillways. *Environ. Fluid Mech.* 9, 427–441.

469 Felder, S., and Chanson, H., 2011. Air–water flow properties in step cavity down a stepped
470 chute. *Int. J. Multiph. Flow*, 37(7), 732-745.

471 Ferziger, J.H., Peric, M., 2012. *Computational methods for fluid dynamics*. Springer Science
472 and Business Media.

473 FLOW-3D[®] User Manual, 2016. FLOW-3D User Manual. Flow Science.

474 Frizell, K.W., Renna, F.M., Matos, J., 2013. Cavitation potential of flow on stepped
475 spillways. *J. Hydraul. Eng.* 139, 630–636.

476 Frizell, K.W., Renna, F.M. and Matos, J., 2015. Closure to “Cavitation potential of flow on
477 stepped spillways”. *J. Hydraul. Eng.*, 141 (8), 07015009.

478 Gonzalez, C. A., and Chanson, H., 2004. Interactions between cavity flow and main stream
479 skimming flows: an experimental study. *Can. J. of Civil Eng.*, 31(1), 33-44.

480 Hirt, C.W., Nichols, B.D., 1981. Volume of fluid (VOF) method for the dynamics of free
481 boundaries. *J. Comput. Phys.* 39, 201–225. doi:10.1016/0021-9991(81)90145-5

482 Hunt, S.L. and Kadavy, K.C. (2010). Energy dissipation on flat-sloped stepped spillways:
483 Part 1. Upstream of the inception point, *Trans. ASABE*, 53(1), 103-109.

484 Issa, R.I., 1985. Solution of the Implicitly Discretized Fluid Flow Equations by Operator-
485 Splitting. *J. Comput. Phys.* 62, 40–65.

486 Launder, B.E. and Sharma, B.I., 1974. Application of the energy-dissipation model of
487 turbulence to the calculation of flow near a spinning disc. *Letters in heat and mass transfer*, 1(2),
488 pp.131-137.

489 Matos, J., 1999. Emulsão de ar e dissipação de energia do escoamento em
490 descarregadores em degraus, Ph.D. Thesis, IST, Portugal (in portuguese).

491 Matos, J., Meireles, I., 2014. Hydraulics of stepped weirs and dam spillways: engineering
492 challenges, labyrinths of research, In "Hydraulic Structures and Society – Engineering
493 Challenges and Extremes", The University of Queensland, Brisbane, Australia, Proc. of the 5th
494 IAHR International Symposium on Hydraulic Structures (ISHS2014), 25-27 June 2014, Brisbane,
495 Australia, H. Chanson and L. Toombes Editors, 30 pp.

496 Meireles, I., 2004. Caracterização do Escoamento Deslizante sobre Turbilhões e Energia
497 Específica Residual em Descarregadores de Cheias em Degraus. M.Sc. thesis, IST, Lisbon,
498 Portugal (in Portuguese).

499 Meireles, I., Matos, J., 2009. Skimming flow in the nonaerated region of stepped spillways
500 over embankment dams. *J. Hydraul. Eng.* 135, 685–689.

501 Meireles, I., 2011. Hydraulics of stepped chutes: experimental-numerical-theoretical study.
502 Ph.D. thesis, Univ. of Aveiro, Portugal.

503 Meireles, I., Renna, F., Matos, J., Bombardelli, F., 2012. Skimming, nonaerated flow on
504 stepped spillways over roller compacted concrete dams. *J. Hydraul. Eng.* 138, 870–877.

505 Meireles, I., Bombardelli, F.A., Matos, J., 2014. Air entrainment onset in skimming flows on
506 steep stepped spillways: an analysis. *J. Hydraul. Res.* 52, 375–385.

507 Menter, F. R., 1993, Zonal Two Equation $k-\omega$ Turbulence Models for Aerodynamic Flows,
508 AIAA Paper 93-2906.

509 OpenFOAM User Guide, 2011. OpenFOAM: The Open Source CFD Toolbox User Guide.
510 The Free Software Foundation Inc.

511 Patankar, S.V., Spalding, D.B., 1972. A calculation procedure for heat, mass and momentum
512 transfer in three-dimensional parabolic flows. *J Heat Mass Transf.* 15, 1787–1806.
513 doi:10.1016/0017-9310(72)90054-3.

514 Renna, F., 2004. Caratterizzazione Fenomenologica del Moto di un Fluido Bifasico lungo
515 Scaricatori a Gradini, Ph.D. thesis, Politecnico di Bari, Cosenza, Italy (in Italian).

516 Roache, P. J., 2009. Fundamentals of verification and validation. Hermosa Publishers, New
517 Mexico, USA.

518 Rodriguez, J. F., Bombardelli, F. A., García, M. H., Frothingham, K. M., Rhoads, B. L., &
519 Abad, J. D., 2004. High-resolution numerical simulation of flow through a highly sinuous river
520 reach. *Water Resources Management*, 18(3), 177-199.

521 Romagnoli, M., Portapila, M., Morvan, H., 2009. Computational simulation of a hydraulic
522 jump (original title, in Spanish: “Simulacion computacional del resalto hidraulico”). *Mec.*
523 *Comput.* XXVIII, 1661–1672.

524 Rusche, H., 2002. Computational fluid dynamics of dispersed two-phase flows at high phase
525 fractions. Imperial College of Science, Technology and Medicine (UK).

526 Schlichting, H., Gersten, K., 2000. Boundary-Layer Theory, 8th Edition. ed. Springer.

527 Shih, T.-H., Liou, W.W., Shabbir, A., Yang, Z., Zhu, J., 1995. A new k - ϵ eddy viscosity
528 model for high reynolds number turbulent flows. *Comput. Fluids* 24, 227–238.
529 doi:10.1016/0045-7930(94)00032-T

530 Sweeney, B.P., 2014. Converged stepped spillway models in OpenFOAM. Kansas State
531 University.

532 Toro, J.P., Bombardelli, F.A., Paik, J., Meireles, I., Amador, A., 2016. Characterization of
533 turbulence statistics on the non-aerated skimming flow over stepped spillways: A numerical
534 study. *Environ. Fluid Mech.* 1–27.

535 Toro, J.P., Bombardelli, F.A. and Paik, J., 2017. Detached eddy simulation of the nonaerated
536 skimming flow over a stepped spillway. *J. of Hydraulic Eng.* 143(9), 04017032.

537 Ubbink, O., 1997. Numerical prediction of two fluid systems with sharp interfaces, PhD
538 Thesis, Imperial College of Science, Technology and Medicine (UK).

539 Van Leer, B., 1977. Towards the ultimate conservative difference scheme III. Upstream-
540 centered finite-difference schemes for ideal compressible flow. *J. Comput. Phys.* 23, 263–275.

541 Witt, A., Gulliver, J., Shen, L., 2015. Simulating air entrainment and vortex dynamics in a
542 hydraulic jump. *Int. J. Multiph. Flow* 72, 165–180.

543 Yakhot, V., Orszag, S., Thangam, S., Gatski, T., Speziale, C., 1992. Development of
544 turbulence models for shear flows by a double expansion technique. *Phys. Fluids Fluid Dyn.*
545 1989-1993 4, 1510–1520.

546 Zhang G, Chanson H (2016a) Hydraulics of the Developing Flow Region of Stepped
547 Spillways. I: Physical Modeling and Boundary Layer Development. *J Hydraul. Eng. ASCE*
548 04016015.

549 Zhang G, Chanson H (2016b) Hydraulics of the Developing Flow Region of Stepped
550 Spillways. II: Pressure and Velocity Fields. J. Hydraul. Eng. ASCE 04016016.
551

552

553 **Figures**

554

555 **Figure 1.** Geometry of the case study and details of the spillway crest zone. Adapted from
556 Bayon et al. (2015).

557

558 **Figure 2.** Experimental stepped spillway facility at the LNEC, used for experimental
559 validation (Matos, 1999; Meireles, 2004, 2011; Renna, 2004).

560

561 **Figure 3.** Detail of mesh of the spillway crest zone.

562

563 **Figure 4.** Water free surface profiles (left) and velocity profiles (right) at $L = 1.04m$ (step
564 23) as a function of mesh element minimum size (Δx), with a first-order upwind scheme, Partial
565 VOF and the RNG $k - \varepsilon$ model, compared against experimental data. Unfilled symbols indicate
566 measurements affected by fluctuations either of the free surface or the inception point position.

567

568 **Figure 5.** Numerical results using RNG $k - \varepsilon$ model and diverse discretization schemes,
569 with a converged mesh size of $\Delta x = 1.5mm$. a) Water free surface profiles; b) Velocity profile
570 at step 23 ($L = 1.04m$); c) Velocity profile within the cavity at $L = 1.072m$. For the
571 experimental data, unfilled symbols indicate measurements affected by either the fluctuations of
572 the free surface or the location of the inception point.

573

574 **Figure 6.** Numerical results using a limited central-difference discretization scheme and
575 diverse turbulence models, with a converged mesh size of $\Delta x = 1.5mm$. a) Water free-surface
576 profiles; b) Velocity profile at step 23 ($L = 1.04m$); c) Velocity profile within the cavity at
577 $L = 1.072m$. For the experimental data, unfilled symbols indicate measurements affected by
578 either the fluctuations of the free surface or the location of the inception point.

579

580 **Figure 7.** Water free-surface profile using RNG $k - \varepsilon$ model and first-order upwind
581 discretization scheme and a converged mesh size of $\Delta x = 1.5mm$ according to type of VOF
582 method: Partial VOF (OpenFOAM) and TruVOF (FLOW-3D®).

583

584 **Figure 8.** Velocity profiles using RNG $k - \varepsilon$ model and a first-order upwind discretization
585 scheme and a converged mesh size of $\Delta x = 1.5mm$ according to type of VOF method: Partial
586 VOF (OpenFOAM) and TruVOF (FLOW-3D®).

587

588 **Figure 9.** Distribution of water depths, boundary-layer development and estimated inception
589 point of air entrainment profile using RNG $k - \varepsilon$ model and a first-order upwind discretization
590 scheme and a converged mesh size of $\Delta x = 1.5mm$ according to type of VOF method: Partial
591 VOF (OpenFOAM) and TruVOF (FLOW-3D) with validation using experimental data and
592 literature.

593

594 **Figure 10.** Velocity and TKE fields throughout the spillway obtained with OpenFOAM
595 using a converged mesh ($\Delta x = 1.5mm$), an upwind first-order discretization scheme and the
596 RNG $k - \varepsilon$ model.

597

598 **Figure 11.** Profiles of normalized velocity, turbulent kinetic energy (TKE), dissipation rate
599 of TKE and pressure at different step edges using RNG $k - \varepsilon$ model and a first-order upwind
600 discretization scheme and a converged mesh size of $\Delta x = 1.5mm$. In the pressure plot, unfilled
601 symbols correspond to pressure profiles 0.32 cm upstream of step edges, where maximum
602 pressure occurs, and p_0 is the hydrostatic pressure at the pseudo-bottom.

603

604 **Figure 12.** Profiles of normalized velocity, turbulent kinetic energy (TKE), dissipation rate
605 of TKE and pressure at different step gaps using RNG $k - \varepsilon$ model and a first-order upwind
606 discretization scheme and a converged mesh size of $\Delta x = 1.5mm$.

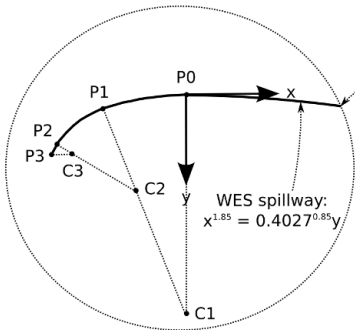
607

608

609

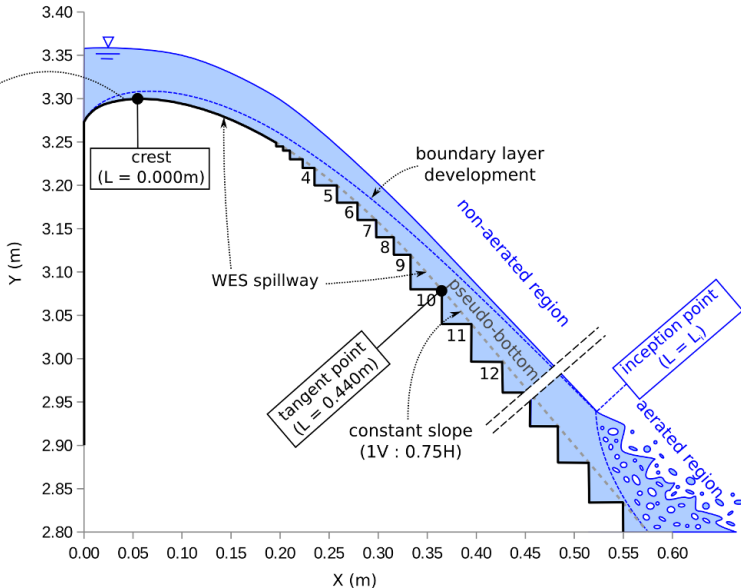
610

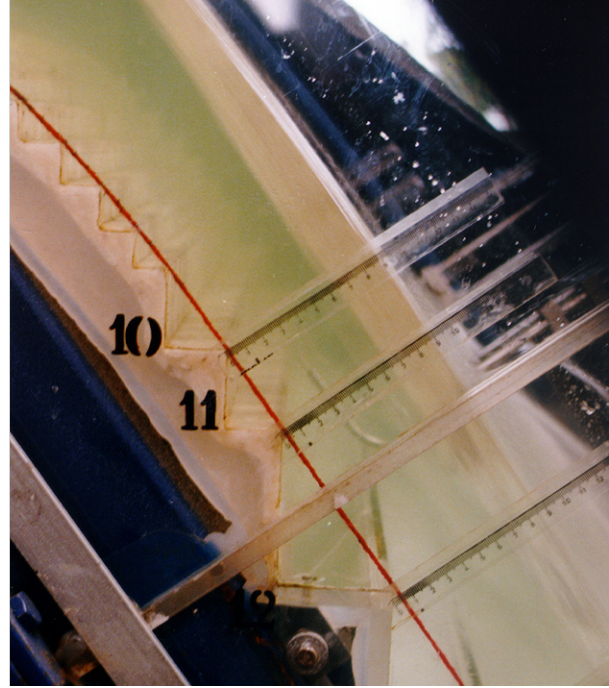
Local Coordinate System (LCS)

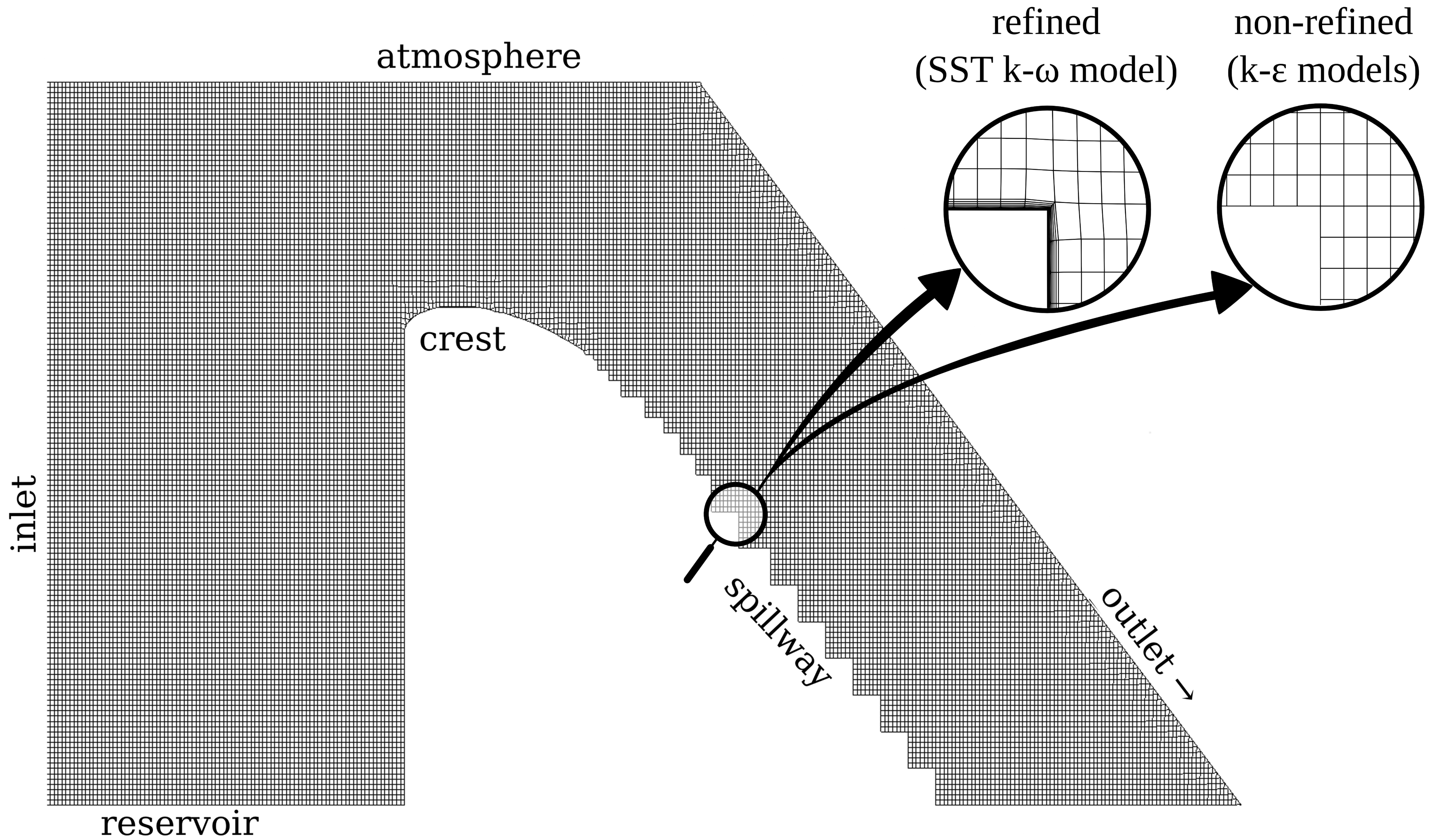


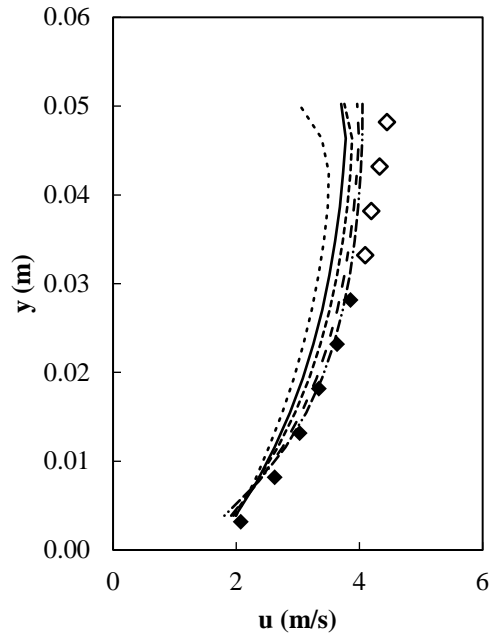
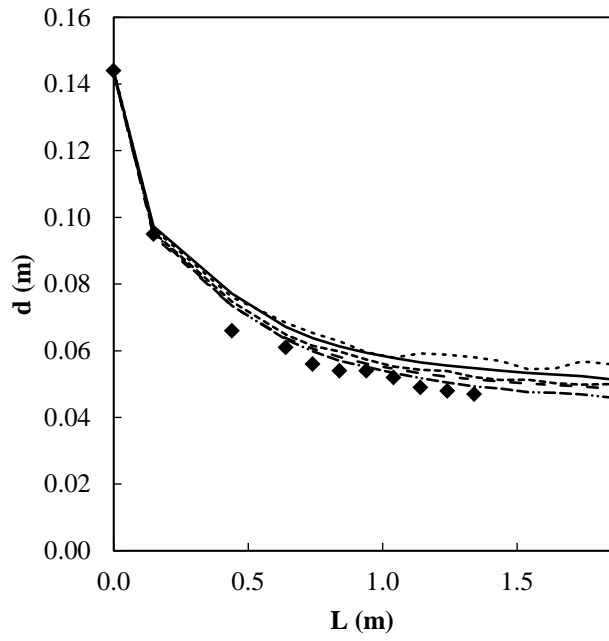
Point	x (m)	y (m)	Arc	radius (m)
P0	0.000	0.000		
P1	-0.035	0.006		
P2	-0.056	0.023		
P3	-0.057	0.027		
C1	0.000	0.101	C1	0.101
C2	-0.021	0.044	C2	0.040
C3	-0.049	0.027	C3	0.008

Global Coordinate System (GCS)

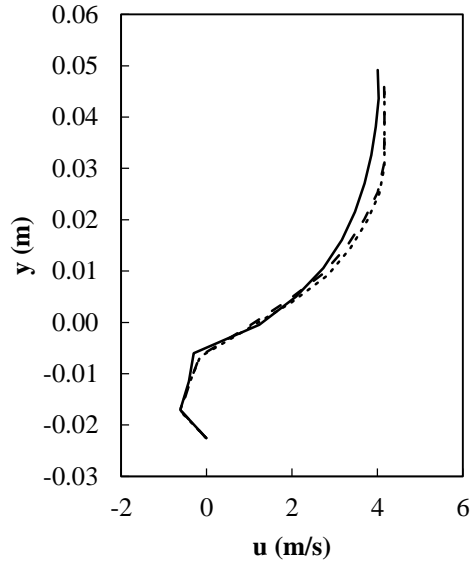
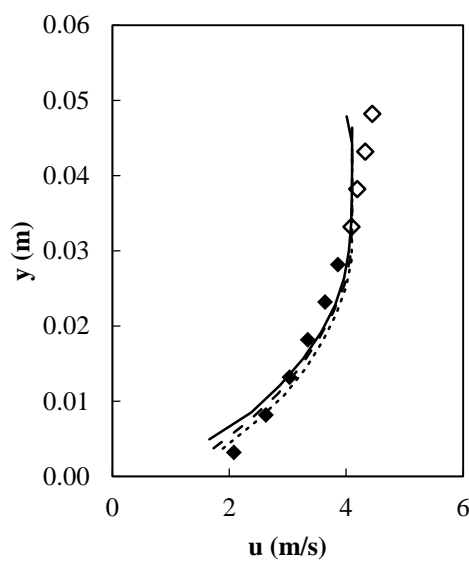
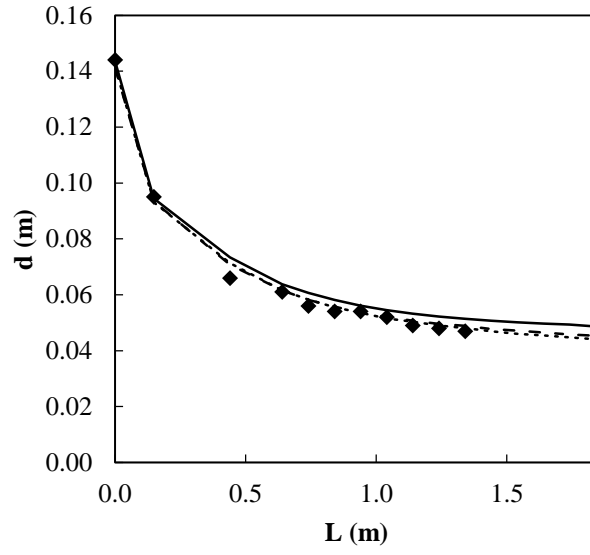




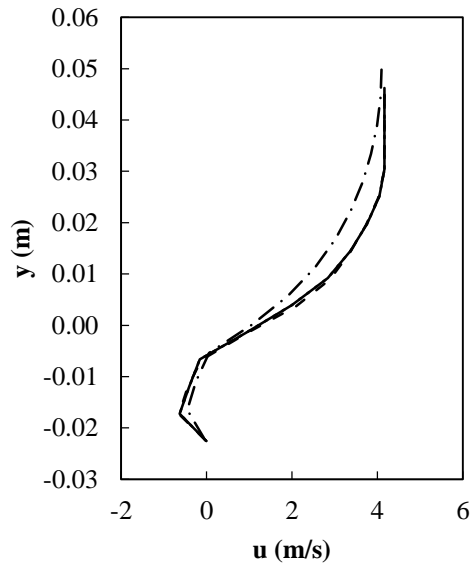
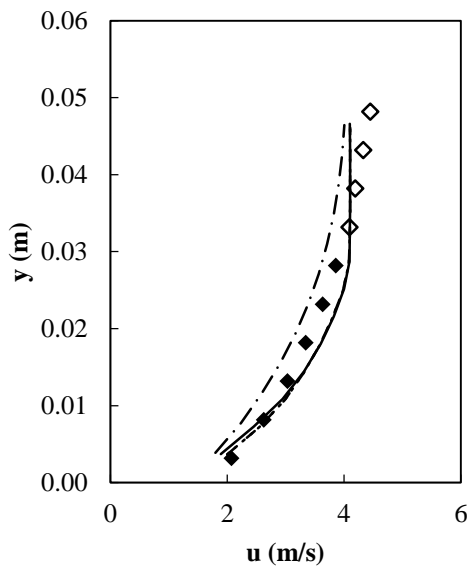
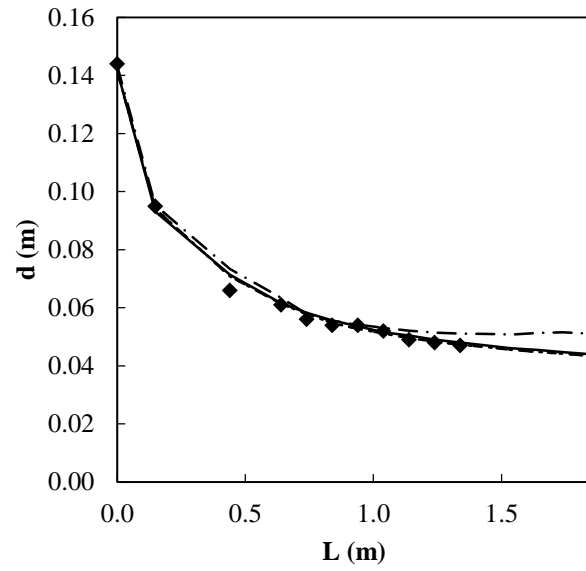




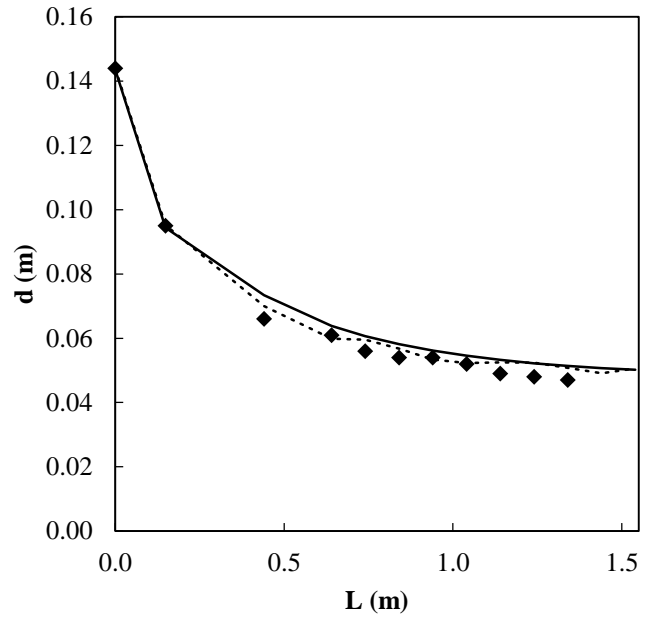
$\cdots\cdots\cdots \Delta x=1.1\text{mm}$
 $-\ - \ \Delta x=1.5\text{mm}$
 $-\ - - - \ \Delta x=2.1\text{mm}$
 $\text{—} \ \Delta x=3.0\text{mm}$
 $\cdots\cdots\cdots \Delta x=4.2\text{mm}$
 \blacklozenge Experimental



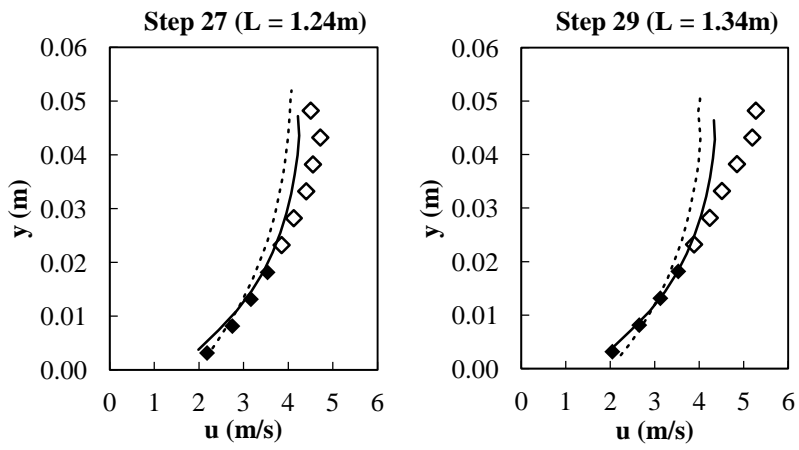
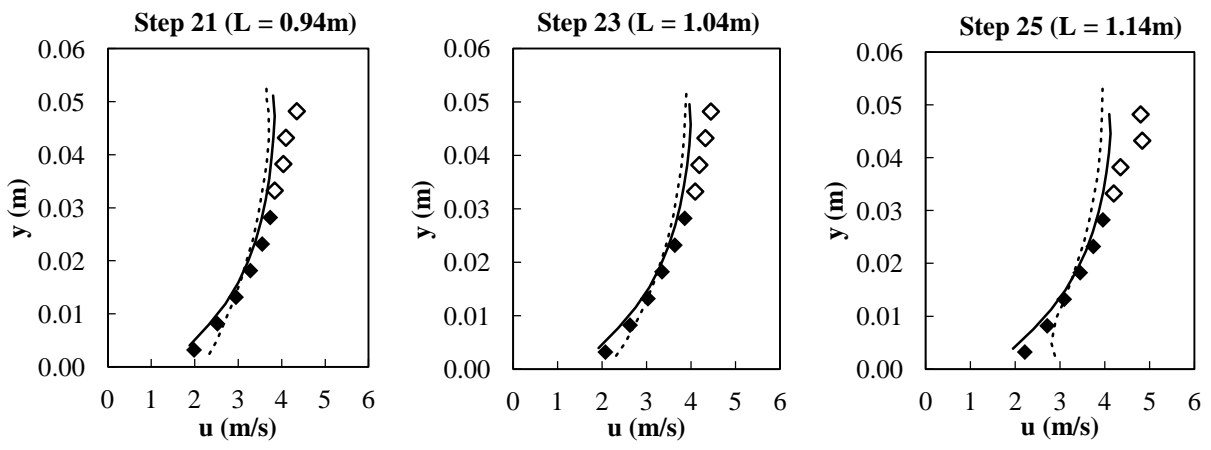
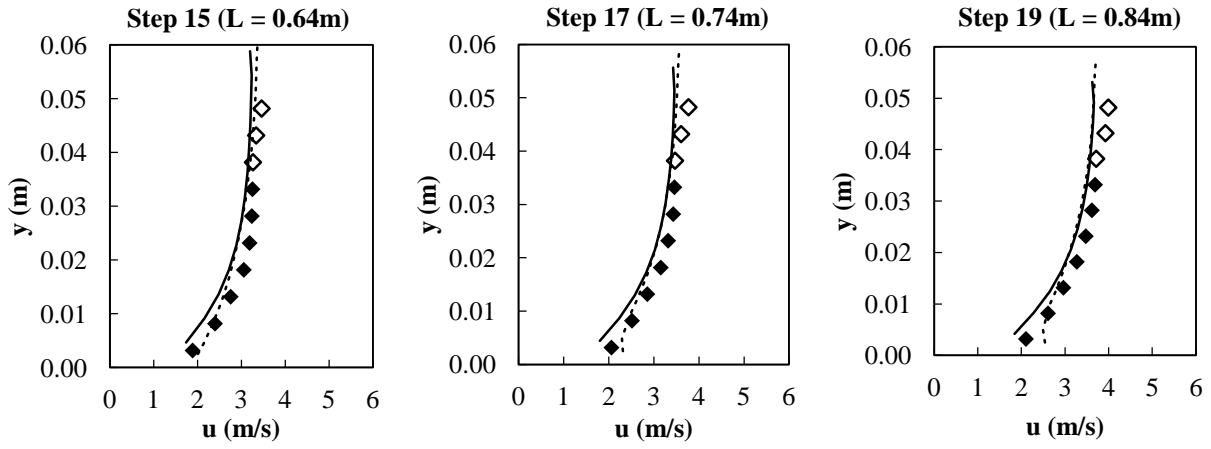
— 1st order upwind Limited Linear - - Van Leer ◆ Experimental



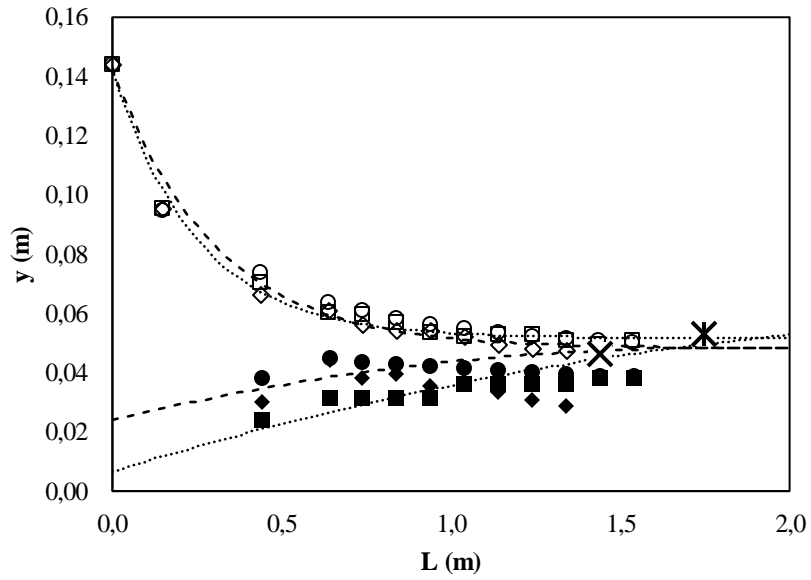
- - - Realizable k- ϵ ——— RNG k- ϵ Standard k- ϵ
 - · - · SST k- ω ◆ Experimental



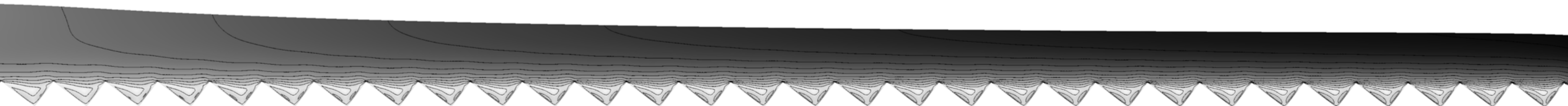
— OpenFOAM FLOW-3D ◆ Experimental



— OpenFOAM ····· FLOW-3D ◆ Experimental

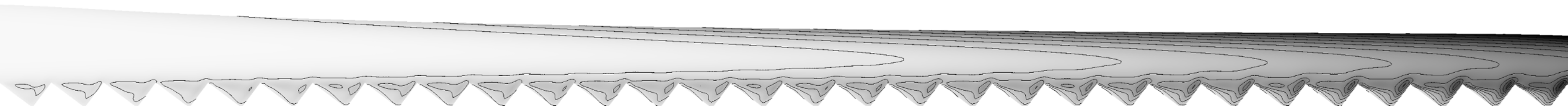
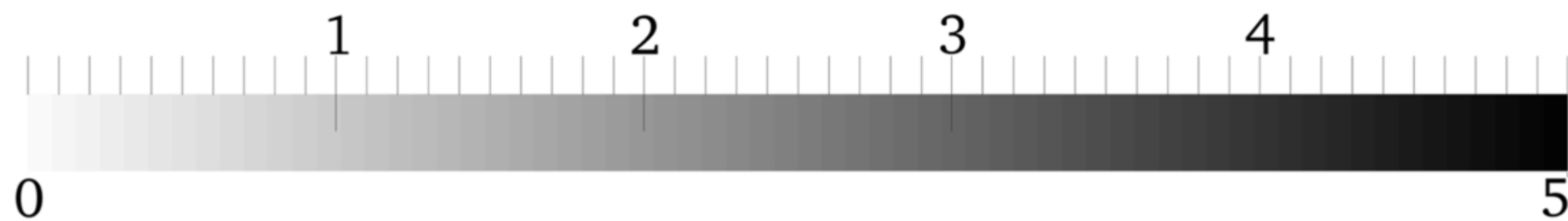


- | | |
|-------------------------|--------------------------------|
| ○ d (OpenFOAM) | ● δ (OpenFOAM) |
| □ d (FLOW-3D) | ■ δ (FLOW-3D) |
| ◇ d (Experimental) | ◆ δ (Experimental) |
| - - - d (OpenFOAM, fit) | - - - δ (OpenFOAM, fit) |
| ⋯ d (FLOW-3D, fit) | ⋯ δ (FLOW-3D, fit) |
| ✕ IP Experimental | ✕ IP Chanson (2002) |



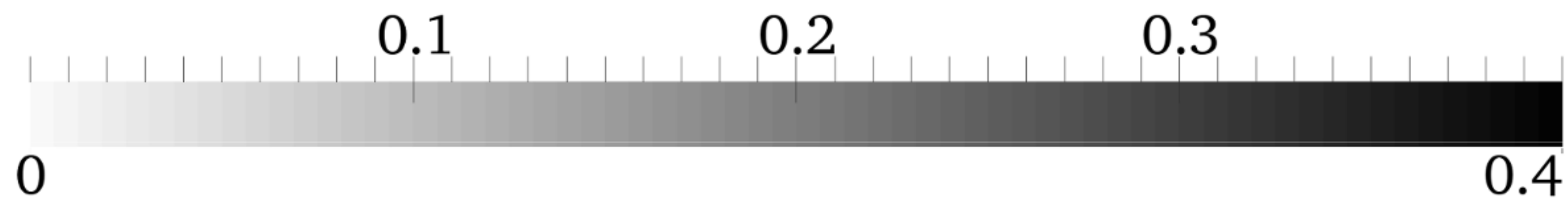
Step	15	20	25	30	35
L(m)	0.64	0.89	1.14	1.29	1.64

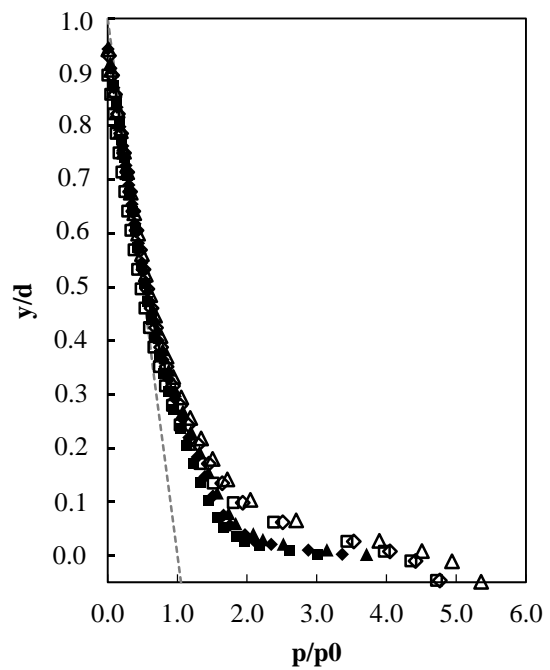
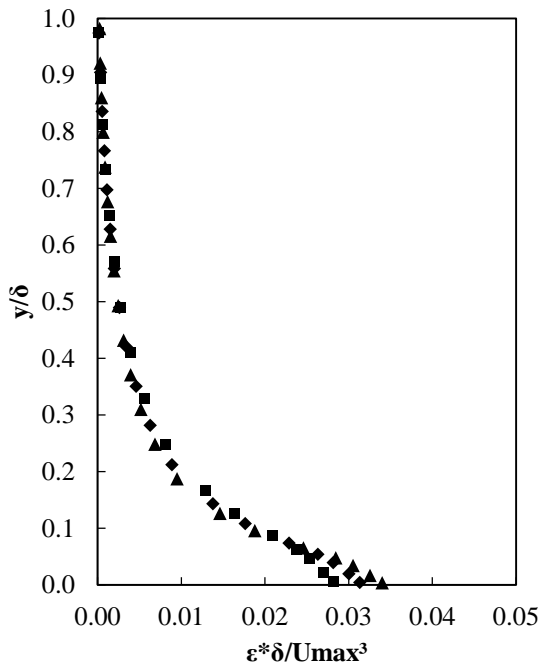
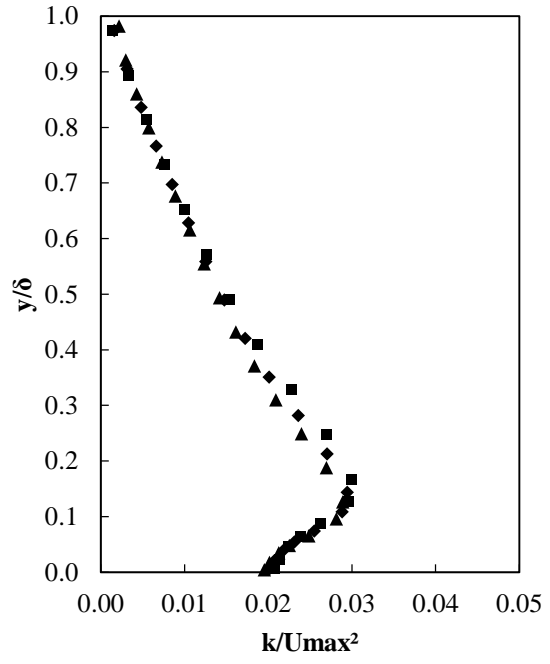
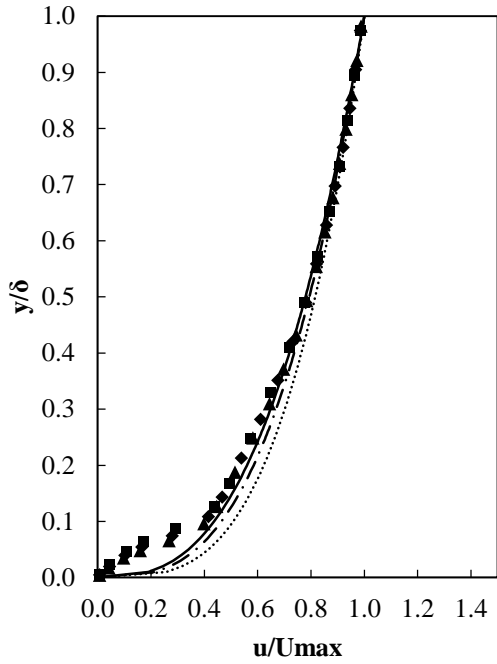
U (m/s)



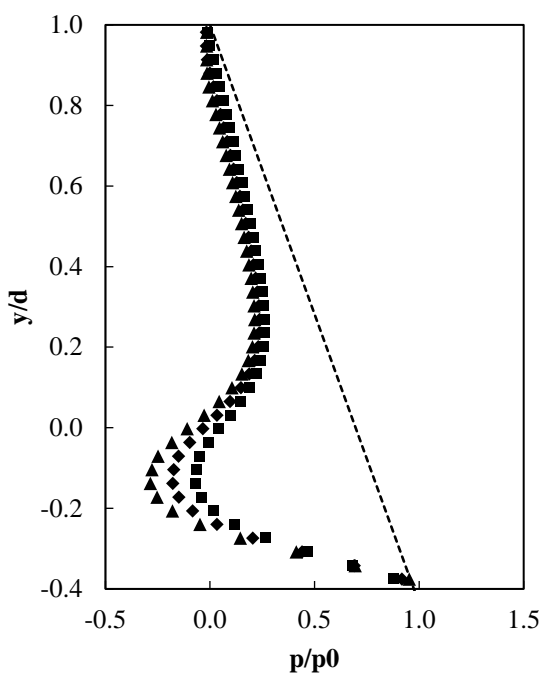
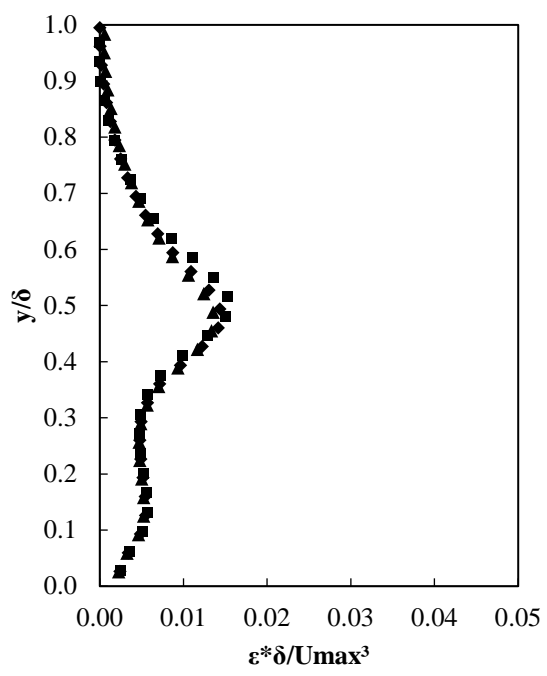
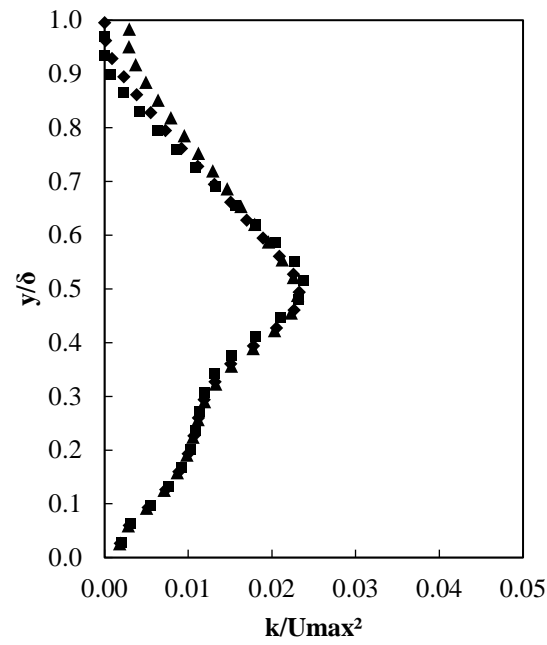
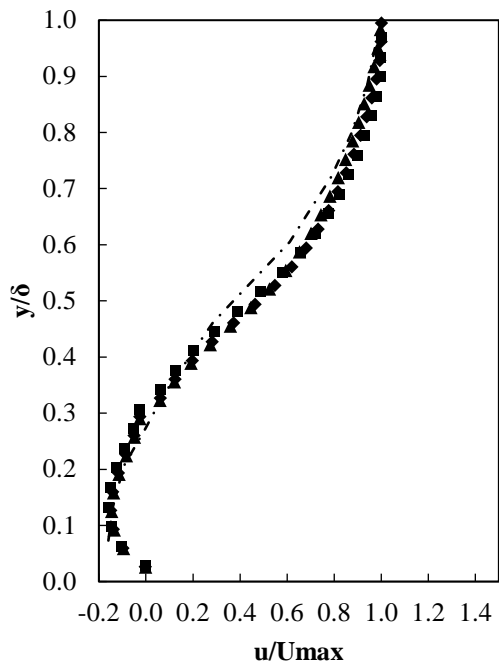
Step	15	20	25	30	35
L(m)	0.64	0.89	1.14	1.29	1.64

k (J/kg)





- Step 19 (L=0.84m)
 - Meireles et al. (2012)
 - CFD
- ◆ Step 23 (L=1.04m)
 - · - · Amador et al. (2006)
- ▲ Step 27 (L=1.24m)
 - - - - Hydrostatic profile



■ $L=0.872m$ ◆ $L=1.072m$ ▲ $L=1.272m$
 - - - - - Hydrostatic - · - · - Amador et al. (2006)